

# Measurements of dynamic forces between drops with the AFM: novel considerations in comparisons between experiment and theory

Grant B. Webber,<sup>\*a</sup> Scott A. Edwards,<sup>b</sup> Geoffrey W. Stevens,<sup>a</sup> Franz Grieser,<sup>c</sup> Raymond R. Dagastine<sup>\*a</sup> and Derek Y. C. Chan<sup>bde</sup>

Received 8th November 2007, Accepted 6th February 2008

First published as an Advance Article on the web 8th April 2008

DOI: 10.1039/b717303b

Dynamic forces between a deformable tetradecane oil drop (radius of curvature  $\approx 25 \mu\text{m}$ ) anchored on the cantilever of the Atomic Force Microscope (AFM) and similar oil drops (radii of curvature 80 to 500  $\mu\text{m}$ ) on the substrate in aqueous electrolyte with added sodium dodecyl sulfate surfactant have been studied. Measurements were made over a range of scan rates that span the range of Brownian velocities of such emulsion drops. The adsorbed anionic surfactants impart a stabilising electrical double layer repulsion between the drops so coalescence was not observed under present conditions. Force–displacement data follow reversible trajectories at low scan rates ( $<0.5 \mu\text{m s}^{-1}$ ) but exhibit increasingly large hysteric effects for scan rates up to  $30 \mu\text{m s}^{-1}$ . The coupling between deformations of the interacting drops and deflections of the AFM cantilever at high scan rates facilitates a self-consistent and independent estimate of the cantilever spring constant if one models variations of cantilever deflection with piezo displacement. In addition to giving excellent agreement between predicted and measured dynamic forces, our model also furnishes quantitative information about: variations of the force with interfacial separation, deformations and velocities of interfaces, pressure distributions in the aqueous film between the drops as well as the absolute separation between the interacting drops. A new dimpling phenomenon is inferred to occur when interacting drops are being separated after the formation of a flattened aqueous film. These new capabilities in the evaluation and interpretation of AFM force measurements overcome a major limitation in the use of the AFM for the absolute quantification of force–separation data.

## 1. Introduction

For close to two decades the atomic force microscope (AFM) has been employed to accurately measure the static interaction forces between well-defined solid surfaces as a function of surface separation down to nanometre separations.<sup>1–5</sup> Such experiments may yield critical, and quantitative, information for simple rigid surfaces *via* comparison with DLVO theory, for example, or with a number of polymer brush theories in the case of coated surfaces. Increasingly, the measurement of colloidal forces between deformable interfaces is of interest, as such interactions are important in industrial and chemical processes such as froth flotation and solvent extraction, in food processing and personal care product formulations, and for many biological functions such as cell–cell interactions. In comparison to interactions involving only rigid surfaces, where the geometries are well-characterised and invariant, deformations of the interface,

both for gas/liquid and liquid/liquid interfaces, render the actual measurements and the subsequent theoretical analysis of the data more complicated.

Advances in AFM experimentation have enabled researchers to probe equilibrium interactions, where approach/retract velocities were below  $\sim 200 \text{ nm s}^{-1}$ , between a rigid particle and a deformable interface, be they liquid/vapor,<sup>6,7</sup> liquid/liquid,<sup>8–14</sup> or polymeric<sup>15,16</sup> interfaces. More recently, these studies have been extended to probe static interactions between two deformable liquid/liquid interfaces.<sup>17</sup> Crucially, corresponding equilibrium theoretical models have been developed to analyze these experiments with some success, garnering qualitative information about the interactions, such as the surface forces and interfacial profiles during deformation.

At higher scan rates time-dependent dynamical effects due to the combination of surface forces, interfacial deformations and hydrodynamic effects become important. Recent experimental force–displacement results for the interactions between both a solid particle and a deformable oil droplet,<sup>18,19</sup> and two deformable oil drops<sup>20–23</sup> in aqueous electrolyte have shown strong hysteric properties. The approach branch of the force–displacement data indicates a strong repulsive interaction whose magnitude increases with increasing scan rate. Along the retraction branch, the force falls off quickly below the approach branch and displays a characteristic attractive minimum whose depth is a function of the scan rate as well as the total displacement. Qualitatively, one can broadly account for these effects in

<sup>a</sup>Department of Chemical and Biomolecular Engineering, Particulate Fluids Processing Centre, The University of Melbourne, Victoria, 3010, Australia. E-mail: gwebber@unimelb.edu.au; rrd@unimelb.edu.au

<sup>b</sup>Department of Mathematics and Statistics, Particulate Fluids Processing Centre, The University of Melbourne, Victoria, 3010, Australia

<sup>c</sup>School of Chemistry, Particulate Fluids Processing Centre, The University of Melbourne, Victoria, 3010, Australia

<sup>d</sup>Department of Mathematics, National University of Singapore, Singapore 117543

<sup>e</sup>Institute of High Performance Computing, 1 Science Park Road, Singapore 117528

terms of hydrodynamic interactions and surface deformations. In this paper, we quantify the interplay between these effects as well as effects due to drop size ratios that range from 3 to 20 by using accurate AFM measurements.

An important and novel approach in the reconciliation of experimental data with a theory that includes effects of surface force, interfacial deformations and thin film hydrodynamics in a consistent way<sup>22</sup> is to compare variations in cantilever deflection with the  $z$ -displacement of the AFM. Such comparisons made it possible to deduce from experimental data both the value of the cantilever spring constant, which can be compared to independent estimates of its value, and the initial separation between the drops. Therefore, the need to account for deformations of the drop in a self-consistent way imposes additional constraints that facilitate the determination of experimental parameters that previously had to be estimated by a separate measurement.

The use of a small drop with radius of curvature of 25  $\mu\text{m}$  that is localised on the tip of a regular tipless V-shaped AFM cantilever ensures that the point of load application on the cantilever can be estimated<sup>14,20,24</sup> and also offers the opportunity to examine the effects of drop size ratio on drop–drop interactions. As we shall see, the agreement in force–displacement results between experiment and theory is very good, so this provides confidence in using the theory to deduce the disposition of the deforming drops such as the degree of deformation, the time dependent drop shapes, and the local instantaneous velocities of the deforming interfaces, and to examine the effects of drop size ratios. Such detailed information on the nanoscale is otherwise inaccessible by current experimental techniques.

This paper is organised as follows. The experimental method is detailed in Section 2 and a brief review of the theoretical model is presented in Section 3. In Section 4 we present analysis of experimental data based on comparing cantilever deflection and piezo position, and demonstrate the spatial variations and time evolutions of the deforming interfaces in the interaction zone, as well as illustrating how the drops deform during dynamical interactions. The paper closes with a discussion of these data in Section 5.

## 2. Experimental method

All interaction data were collected using an Asylum MFP-3D atomic force microscope (Asylum Research, Santa Barbara, USA) with a fluid cell attachment. All fluid cell components (o-rings, membranes, *etc.*) were rinsed with ethanol (AR-Grade, Sigma Aldrich, used as received) and dried under purified nitrogen stream before assembly in a laminar flow cabinet. The spring constant of tipless V-shaped silicon nitride NP-O cantilevers (Veeco Probes, CA) was measured using the thermal tune function of the MFP-3D software, which utilises the equations of Hutter and Bechhoefer.<sup>25</sup> The cantilevers and one half of the glass slide bottom substrate were sputter coated (Emitech K575X, UK) with chromium ( $\sim 2$  nm) and then gold ( $\sim 10$  nm), and immediately hydrophobised by immersion in decanethiol solution ( $\sim 10$  mM in ethanol, Sigma Aldrich, used as received) for at least 18 hours.<sup>26</sup> The decanethiol does not form a stable self-assembled monolayer (SAM) on the uncoated half of the glass substrate, and consequently this part of the

substrate is less hydrophobic. Both the slide and cantilever were carefully rinsed with ethanol and dried under nitrogen prior to assembly in the fluid cell. An array of tetradecane (Sigma Aldrich, purified by passing through a magnesium silicate column) droplets was immobilised on the glass substrate by aspiration through a narrow gauge syringe-mounted needle, as described by Dagastine *et al.*<sup>11</sup> The tetradecane droplets were immersed in an aqueous solution of 5 mM sodium dodecyl sulfate (SDS, Sigma Aldrich, used as received) by careful injection. The cantilever was then mounted in the tip holder, and the fluid cell installed into the AFM.

At the beginning of the experiment the cantilever was manually lowered into contact with a tetradecane droplet immobilised on the uncoated section of the glass substrate. Due to the higher affinity for the hydrophobised tip, the tetradecane droplet remained attached to the tip as it was raised away from the substrate. By selecting a small tetradecane droplet to “pick up” in this manner, it was possible to ensure that the tip-immobilised droplet only contacted the end triangle of the cantilever. That is, no tetradecane spread onto the legs of the cantilever. This facilitates an accurate determination of the radius of curvature of the tip-immobilised droplet using the same methodology as for the surface-immobilised droplet, as detailed below. The cantilever was then positioned above a drop immobilised on the sputter-coated section of the substrate. In this way the interactions between a single tip-immobilised drop and surface-immobilised drops of three different sizes were characterised. Care was taken to ensure that the drops were aligned such that the movement was along the surface normal through the apices of the interacting drops. This ensures that deformations of the drops were axisymmetric and facilitates a simpler theoretical analysis.

The base contact radii of the drops on the cantilever,  $r_c$  and substrate,  $r_s$  were measured using optical microscopy. The undistorted radii of curvature for the drops,  $R_{oc}$  and  $R_{os}$  respectively, were then calculated from the (acute) contact angle,  $\theta$  of tetradecane on a decanethiol SAM in 5 mM SDS solution using the geometric relations:  $R_{oc} = r_c/\sin \theta$  and  $R_{os} = r_s/\sin \theta$ , as effects of gravity are negligible. The contact angle of macroscopic drops of tetradecane on a decanethiol SAM were measured separately using a DataPhysics OCA 20 Tensiometer, and this value of contact angle was applied to the microscale droplets of the AFM experiment. Variability in the contact angle due to drop hysteresis is estimated to be less than 5%, and the theory has been shown previously to be insensitive to changes in the contact angle.<sup>23</sup> In the theoretical framework described below the contact line of the drop is assumed to be pinned, though the value of the contact angle is allowed to vary as a result of deformations in the drops. The interfacial tension was measured *via* the pendant drop method using the same system.

A schematic representation of the AFM configuration used in these experiments is shown in Fig. 1. It should be noted that in the Asylum MFP-3D AFM the  $z$ -axis piezo-electric crystal is mounted in the tip holder, and consequently it is the cantilever that moves during the collection of force–distance data. From Fig. 1 it is evident that due to interactions between the two drops, changes in the piezo displacement  $\Delta X(t)$  give rise to changes in the separation  $h(r,t)$  between the drops, the degree of deformation in the profiles  $z_c(r,t)$  and  $z_s(r,t)$  of each drop and the

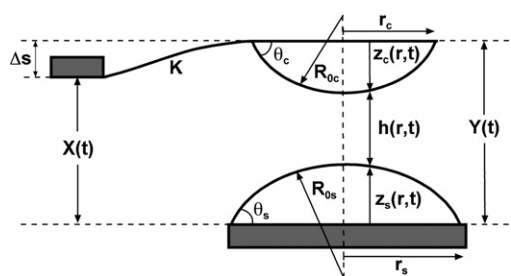


**Fig. 1** Schematic diagram of the AFM drop-drop configuration that shows key elements of the apparatus: cantilever deflection,  $\Delta s$ , drop heights  $z_c(r,t)$  and  $z_s(r,t)$ , contact angles  $\theta_c$  and  $\theta_s$ , drop base contact radii  $r_c$  and  $r_s$ , unperturbed drop radius of curvature,  $R_{oc}$  and  $R_{os}$ , of the two drops on the cantilever and on the substrate as well as the separation  $h(r,t)$  between the surfaces of the drops.

deflection of the cantilever,  $\Delta s(t)$ . Experimentally,  $\Delta X(t)$  is specified but the absolute value of  $X$  is not known *a priori*. It is customary to assign an arbitrary origin for  $X$ , and display the measured force,  $F(\Delta X)$  as a function of the change in displacement  $\Delta X$  relative to this origin.<sup>27</sup> As such, the displayed data are offset horizontally to allow clear comparison of important features. Such force vs. displacement data, over a full approach and retract cycle, were recorded for a range of cantilever speeds or scan rates from  $50 \text{ nm s}^{-1}$  to  $30 \text{ }\mu\text{m s}^{-1}$ , though for reasons of clarity only a selection of these data is displayed. For quantitative comparison with theory (see later), we choose the value  $X = 0$  to be the position where the two drops would touch if they did not deform.

In a typical force-displacement cycle over the time interval,  $0 < t < t_{\text{max}}$  (see Fig. 2), the piezo-electric drive is set to drive the cantilever towards the substrate by decreasing  $X(t)$  for a set distance—this is called the *approach* phase. The piezo-electric drive is then reversed to drive the cantilever away from the substrate by increasing  $X(t)$  by the same amount—this is called the *retract* phase. During a full approach and retract cycle the motion is set by software to be driven at a nominal constant speed called the scan rate that can be varied from  $50 \text{ nm s}^{-1}$  to  $30 \text{ }\mu\text{m s}^{-1}$ . On the Asylum MFP-3D AFM the piezo drive is

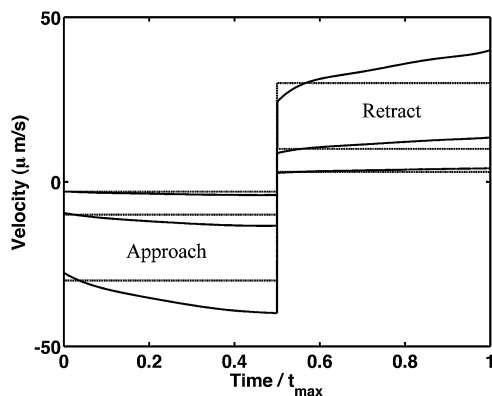


**Fig. 2** The actual scan rate or  $dX/dt$  (continuous lines) of the cantilever as derived from LVDT data for nominal scan rates (broken lines) of  $3 \text{ }\mu\text{m s}^{-1}$ ,  $10 \text{ }\mu\text{m s}^{-1}$ , and  $30 \text{ }\mu\text{m s}^{-1}$ . The time is scaled by the maximum drive-time  $t_{\text{max}}$  which varies for each scan rate. The approach part of the cycle corresponds to  $dX/dt < 0$  and the retract part of the cycle to  $dX/dt > 0$ .

operated in an open loop control configuration but the non-linear nature of the piezo actuator results in deviations from the desired scan rate. However, the AFM is equipped with a linear variable differential transformer (LVDT) sensor which reports the actual location of the  $z$ -piezo as it moves through the approach/retract cycle of a force-displacement measurement. The time dependence of the position of the  $z$ -piezo  $X(t)$  as well as  $dX(t)/dt$  can be obtained from the system software.<sup>19</sup> In our theoretical modeling, these outputs will be used in boundary conditions in the governing equations of our model to obtain results that can be compared with experimental data and to extract force-separation information. Examples of the form of the (non-constant) drive velocity  $dX(t)/dt$  for different typical scan rates are given in Fig. 2.

### 3. Model

The theoretical model comprises the following physical elements. The colloidal force between the tetradecane drops is dominated by electrical double layer repulsion that arises from surface charges due to adsorbed anionic surfactants. The disjoining pressure  $\Pi(h)$  due to this interaction is calculated with the Poisson-Boltzmann theory using measured surface potentials and is taken to be a function only of the instantaneous local separation  $h(r,t)$ , between the surfaces of the interacting drops. Implicit in this is the assumption that the variation of the separation, which is on the scale of nanometres, takes place slowly over a radial scale  $r$  of the order micrometres and that the double layer maintains equilibrium as the drops move towards and away from each other. The interfacial tension,  $\sigma$  of the SDS populated tetradecane/electrolyte interface was measured independently. At the surfactant concentration used, the adsorbed surfactant layer is expected to be closely packed so surfactant transport along, or out of, the oil/water interface during interaction is not expected to be significant and so the interfacial tension is assumed to be constant at any given surfactant concentration. The Young-Laplace equation, augmented by pressure contributions from hydrodynamics and disjoining pressures, is used to describe deformations of the oil/water interface. The capillary number of the system,  $Ca = \mu V/\sigma$ , which measures the ability of hydrodynamic forces arising from flow in the aqueous phase (with constant shear viscosity  $\mu$ ) to overcome surface tension forces of the drop, is less than  $10^{-5}$ . Thus, as we shall see, while dynamic effects may be large, the spatial extent of drop deformations remains small on the scale of the drops. The drops maintain constant volume during interaction—this is an important physical constraint that has not been imposed in other theoretical treatments in the literature. This constraint provides a key boundary condition to the governing equations and takes into account the small but important deformations in the interacting drops in the region outside the interaction zone between the drops. All parameters needed in the theory are measured independently and, as indicated earlier, the comparison of experimental variations in cantilever deflection data with  $z$ -piezo displacement to theory provides an additional check on the measured spring constant of the cantilever.

The derivation of the governing equations has been given earlier,<sup>22,28</sup> we provide a summary here. As particular care was

taken to align the centre of symmetry of the interacting drops, the variation of the thickness,  $h(r,t)$ , of the aqueous film between the drop surfaces can be assumed to be axisymmetric. In the range of scan rates used, fluid motion is in the Stokes regime and the Reynolds lubrication theory of film drainage can be used to describe the time evolution of the film thickness  $h(r,t)$  and its dependence on the hydrodynamic pressure  $p(r,t)$ :

$$\frac{\partial h(r,t)}{\partial t} = \frac{1}{12\mu r} \frac{\partial}{\partial r} \left( r h^3(r,t) \frac{\partial p(r,t)}{\partial r} \right) \quad (1)$$

Implicit in this equation is the assumption that the no-slip or 'stick' or immobile boundary condition applies at the surfactant populated tetradecane/electrolyte interface. At the surface coverage of surfactants in our experiments we expect this assumption to be valid.<sup>29–31</sup> This no-slip boundary condition also means that possible fluid motion inside the oil drops does not play a role in the hydrodynamic interaction.

The shape of the drop on the cantilever,  $z_c(r,t)$ , and on the substrate,  $z_s(r,t)$ , (see Fig. 1) is governed by the axisymmetric Augmented Young–Laplace equation

$$\frac{\sigma_c}{r} \frac{\partial}{\partial r} \left( \frac{r(\partial z_c/\partial r)}{(1 + (\partial z_c/\partial r)^2)^{1/2}} \right) = -\frac{2\sigma_c}{R_c} + (p(r,t) + \Pi(h(r,t))) \quad (2a)$$

$$\frac{\sigma_s}{r} \frac{\partial}{\partial r} \left( \frac{r(\partial z_s/\partial r)}{(1 + (\partial z_s/\partial r)^2)^{1/2}} \right) = -\frac{2\sigma_s}{R_s} + (p(r,t) + \Pi(h(r,t))) \quad (2b)$$

where we allow for the possibility of different interfacial tensions for the drops on the cantilever and the substrate,  $\sigma_c$  and  $\sigma_s$ , respectively. The Laplace pressure of each drop  $\Delta P_c \equiv (2\sigma_c/R_c)$  and  $\Delta P_s \equiv (2\sigma_s/R_s)$  are determined by the constant volume constraint on each drop. As we shall see, the lengths  $R_c$  and  $R_s$  that characterise the Laplace pressure of each drop are very close to the measured undistorted radii of curvature  $R_{oc}$  and  $R_{os}$  of the drops. In the region where the drops interact for which  $(\partial z_c/\partial r)^2 \ll 1$  and  $(\partial z_s/\partial r)^2 \ll 1$ , the quadratic terms in the denominators in eqn (2a),(b) are small and may be neglected. From the geometry of the apparatus (Fig. 1), the distance  $Y(t)$

$$Y(t) \equiv X(t) + \Delta s(t) = h(r,t) + z_c(r,t) + z_s(r,t) \quad (3)$$

and the cantilever deflection  $\Delta s(t)$  are both independent of  $r$ , so the required equation that describes the film thickness as a result of hydrodynamic and disjoining pressures can then be found by adding eqn (2a) and eqn (2b) and then using eqn (3) to give

$$\frac{\sigma}{2r} \frac{\partial}{\partial r} \left( r \frac{\partial h}{\partial r} \right) = \frac{2\sigma}{R} - (p + \Pi) \quad (4)$$

where we have defined  $R$  by  $1/R \equiv \frac{1}{2} (1/R_c + 1/R_s)$  and  $\sigma$  by  $1/\sigma \equiv \frac{1}{2} (1/\sigma_c + 1/\sigma_s)$ .

Equations (1) and (4) are to be solved in the domain  $0 < r < r_{\max}$  with initial undistorted film thickness:  $h(r, t_{\text{init}}) = h_{\text{init}} + r^2/R_o$ , where  $R_o$  is defined as defined above with the unperturbed

radii of curvature:  $R_{oc}$  and  $R_{os}$ . At  $r = 0$ , the usual conditions required by symmetry considerations apply:  $(\partial h/\partial r) = 0$ ,  $(\partial p/\partial r) = 0$ . The value of  $r_{\max}$  is chosen so that for  $r > r_{\max}$ , the film thickness  $h$  is sufficiently large that the effects of the disjoining pressure  $\Pi(h)$  will be negligible. We impose the known limiting form of pressure  $p \sim r^{-4}$  in the form  $4p + r(\partial p/\partial r) = 0$  at  $r_{\max}$ .<sup>32</sup> The force,  $F$  is calculated from the following integral:

$$F(t) = 2\pi \int_0^{\infty} [p(r,t) + \Pi(r)] r dr \quad (5a)$$

$$= 2\pi \int_0^{r_{\max}} [p(r,t) + \Pi(r)] r dr + 2\pi \int_{r_{\max}}^{\infty} p(r,t) r dr \quad (5b)$$

where the second integral for  $F(t)$  in eqn (5b) may be evaluated using the asymptotic form of  $p$ .

A final boundary condition at  $r_{\max}$  follows from imposing a constant volume constraint on each interacting drop. Outside the interaction zone,  $r > r_{\max}$ , both drop shapes have the following asymptotic form that follows from the constant volume constraint<sup>33,34</sup>

$$z_\alpha(r,t) \cong z_{o\alpha} - \frac{r^2}{2R_{o\alpha}} + \frac{F(t)}{2\pi\sigma_\alpha} \left[ \log\left(\frac{r}{2R_{o\alpha}}\right) + B(\theta_\alpha) \right] + \dots \quad (6)$$

where  $\alpha = c$  or  $s$  for drops on the cantilever or substrate,  $R_{o\alpha}$  is the corresponding undistorted radius of curvature at the drop apex and  $z_{o\alpha}$  is the unperturbed drop height. The omitted terms in eqn (6) are smaller by a factor  $F/\sigma R_o$ . The expression for  $B(\theta)$  in terms of the equilibrium contact angle  $\theta$  of the undistorted drop depends on whether the three phase contact line (TPL) of the drop is *pinned* (so the contact angle will deviate from the equilibrium value) or is *unpinned* (and is free to move along the surface to maintain the contact angle at the equilibrium value) during interaction:

$$B(\theta) = \begin{cases} 1 + \frac{1}{2} \log\left(\frac{1 + \cos\theta}{1 - \cos\theta}\right), & \text{pinned TPL} \\ 1 + \frac{1}{2} \log\left(\frac{1 + \cos\theta}{1 - \cos\theta}\right) - \frac{1}{2 + \cos\theta}, & \text{unpinned TPL} \end{cases} \quad (7)$$

The drop shapes, film thickness and  $z$ -piezo displacement are related by the geometric condition in eqn (3) (see Fig. 1) where the cantilever deflection  $\Delta s(t)$  and the force  $F(t)$  are related by the spring constant,  $K$  of the cantilever

$$F(t) = K\Delta s(t) \quad (8)$$

The final boundary condition can now be obtained by differentiating eqn (3) with respect to  $t$ , and evaluating it at  $r = r_{\max}$  where the large  $r$  asymptotic expressions for the drop shape in eqn (6) may be used. This gives

$$\frac{dX}{dt} = \frac{\partial h}{\partial t} + C \frac{dF}{dt}, \quad \text{at } r = r_{\max} \quad (9a)$$

with

$$C = \frac{1}{2\pi\sigma_c} \left[ \log\left(\frac{r_{\max}}{2R_{oc}}\right) + B(\theta_c) \right] + \frac{1}{2\pi\sigma_s} \left[ \log\left(\frac{r_{\max}}{2R_{os}}\right) + B(\theta_s) \right] - \frac{1}{K} \quad (9b)$$

This completes the specification of the governing equations and boundary conditions. Equations (1), (4), (5a,b) and (9a,b) are cast as a set of coupled differential-algebraic equations to be solved for the force and the film thickness as functions of position and time.<sup>22</sup> The drop profiles and interfacial velocities can then be obtained from eqn (2a,b). We work with directly measurable quantities, namely, the cantilever deflection and the *z*-piezo displacement when comparing experiment with theory rather than comparing the force, which is a derived quantity, so that any experimental uncertainties concerning the measured value of the cantilever spring constant can be accommodated. Multiple sets of cantilever deflection *vs.* *z*-piezo displacement

**Table 1** Values of key parameters of the system that have been measured or taken from the literature

Parameters	As measured	Model
Radius of contact line of drop on cantilever, $r_c/\mu\text{m}$	$18 \pm 2$	19
Radius of contact line of drops on substrate, $r_s/\mu\text{m}$	Drop S: $61 \pm 2$ Drop M: $108 \pm 2$ Drop L: $392 \pm 2$	61 108 392
Radius of curvature of drop on cantilever, $R_{oc}/\mu\text{m}$	$24 \pm 7$	25
Radius of curvature of drops on substrate, $R_{os}/\mu\text{m}$	Drop S: $80 \pm 12$ Drop M: $141 \pm 15$ Drop L: $513 \pm 60$	80 141 513
Cantilever spring constant, $K/\text{N m}^{-1}$	$0.093 \pm 10\%$	0.098
Surface potential of drops <sup>31</sup> /mV	$-100 \pm 10$	-100
Interfacial tension, $\sigma/\text{mN m}^{-1}$	$10 \pm 2$	Drop S: 11 Drop M: 9.5 Drop L: 9.0
Contact angles, $\theta/^\circ$ (cantilever and substrate)	$50 \pm 10, 50 \pm 5$	50, 50
SDS concentration/mM	5	5

data taken on the same cantilever are fitted with the same spring constant. Displacements  $X(t)$  and instantaneous velocities  $dX/dt$  as obtained from the LVDT data (Fig. 2) will be used as input to the boundary condition at  $r_{\max}$  as given by eqn (9a,b).

## 4. Results

Relevant experimental parameters, either determined in this work or taken from the literature are summarised in Table 1. The drop on the cantilever has an estimated undistorted radius of curvature of  $24 \mu\text{m}$ . Three drops on the substrate of varying undistorted radii of curvature  $R_{os}$  labeled small (S:  $R_{os} = 80 \mu\text{m}$ ), medium (M:  $R_{os} = 141 \mu\text{m}$ ) and large (L:  $R_{os} = 513 \mu\text{m}$ ) were used to give drop size ratios that ranged from around 3 to 20.

In Fig. 3, the “as measured” values of system parameters listed in Table 1 were used to calculate the cantilever deflection  $\Delta s$  as a function of the cantilever displacement  $\Delta X$  at a scan rate of  $30 \mu\text{m s}^{-1}$  for the three different sized drops on the substrate. To facilitate comparison with earlier work, we also show the corresponding force obtained from  $F = K\Delta s$ . The zero of  $\Delta X$  is taken to be the position where the drops would have made contact if they did not deform and the displacement function  $\Delta X(t)$  is obtained from the LVDT output. The value of the initial distance of closest approach between the two drops  $h_{\text{init}}$  in each case has to be assumed as this cannot be measured accurately on the AFM. Values of  $h_{\text{init}}$  between  $1.7 \mu\text{m}$ – $1.9 \mu\text{m}$  fit the experimental data (see Fig. 3) and are consistent with experimental estimates. The position of the attractive minimum on the retract branch is a feature of the force curves that is sensitive to the value of  $h_{\text{init}}$ . For each deflection–displacement run, the maximum travel,  $\Delta X_{\text{max}}$ , of the piezo is set by the AFM controlling software. From the LVDT data,  $\Delta X_{\text{max}}$  is  $2.4 \pm 0.1 \mu\text{m}$  for all runs. The maximum cantilever deflection or force varies with the combined effects of the initial distance of closest approach,  $h_{\text{init}}$ , between the surfaces of the drops and the maximum travel,  $\Delta X_{\text{max}}$ , of the piezo displacement. The depth of the attractive minimum on retraction is a sensitive function of the scan rate (see Fig. 4). With all other parameters being equal, a larger drop ratio gives rise to a larger hysteric loop in the deflection–displacement curve because the lower Laplace pressure of the large drop makes it more deformable.

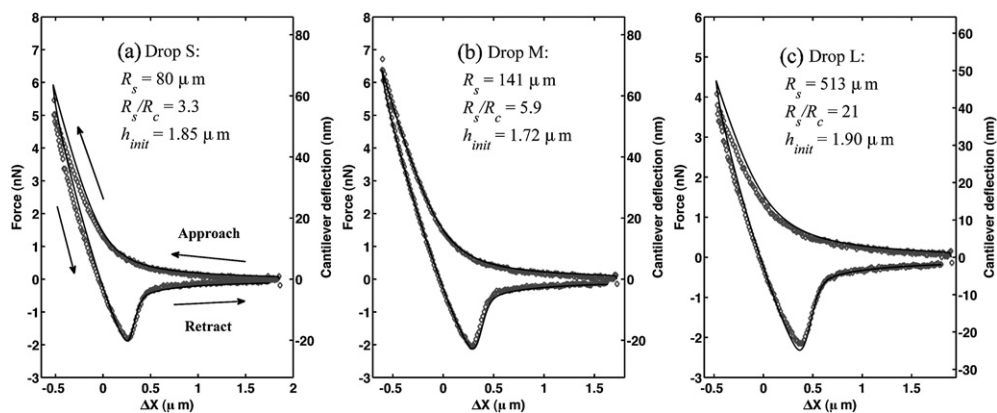


**Fig. 3** Comparison of the cantilever deflection  $\Delta s$  and force  $F$  versus cantilever displacement,  $\Delta X$ , between experiment and theory (smooth line) using “as measured” values of system parameters in Table 1 for three different drop sizes  $R_{os}$  on the substrate. The radius of curvature of the drop on the cantilever was taken to be  $R_{oc} = 24 \mu\text{m}$ , the scan rate was  $30 \mu\text{m s}^{-1}$ . The initial separation  $h_{\text{init}}$  used in each case is indicated in the figure.

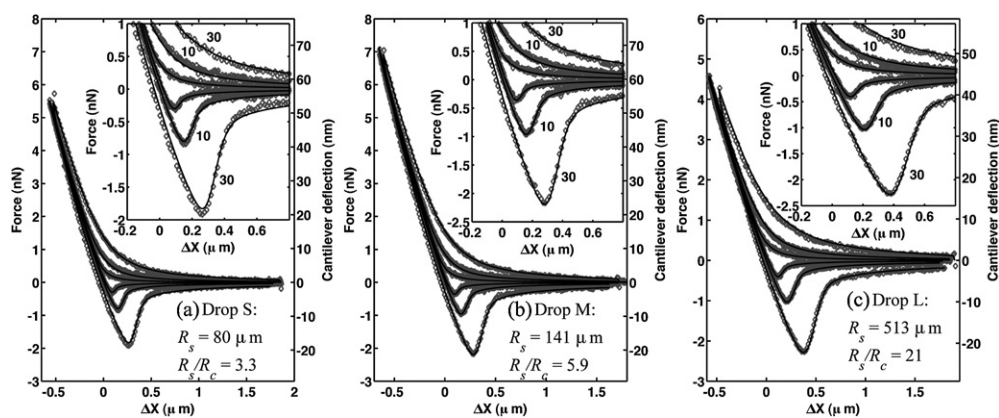


**Fig. 4** Comparison of the cantilever deflection  $\Delta s$  and force  $F$  versus cantilever displacement  $\Delta X$  between experiment and theory (smooth line) using “Model” values of system parameters (see Table 1) for three different drop sizes  $R_{os}$  on the substrate. The initial separations  $h_{init}$  are given in Table 2. The scan rates are 1, 3, 10 and  $30 \mu\text{m s}^{-1}$  in each case.

While the agreement between experiment and theory in Fig. 3 is acceptable this can be improved by adjusting system parameters within the measurement tolerances given in Table 1. By making small changes as indicated in the “Model” column in Table 1, based on optimising the theory to the experimental data comparison at the scan rate of  $30 \mu\text{m s}^{-1}$ , we then used these same changes to compare experiment and theory in the entire suite of other scan rates from  $1 \mu\text{m s}^{-1}$  to  $30 \mu\text{m s}^{-1}$  in Fig. 4. We found it necessary to vary the SDS populated tetradecane/electrolyte interfacial tension (for both drops having the same interfacial tension) for each of the three drop-size ratios given in Table 1, though the required variations in the interfacial tension remain within experimental tolerance of  $10 \pm 2 \text{ mN m}^{-1}$ . A slight adjustment in the value of the cantilever spring constant, again within measurement tolerance, for all data sets improved the agreement. Recently, we have shown that the distributed load on the cantilever may have a small effect on the effective spring constant,<sup>24</sup> but in this instance, the fitted spring constant value is well within the experimental error of the calibration method. The only change made for each scan rate was the initial distance of closest approach  $h_{init}$  between the two drops. Each set of data is an individual measurement and due to thermal drift in the instrument one would expect  $h_{init}$  to be similar, but not constant between measurements. The advantage of this model is that it is a way to determine  $h_{init}$ , which varied over a small interval of less than  $\pm 0.5 \mu\text{m}$  for these data. The exact value of  $h_{init}$  for each case is given in Table 2. With these small but justifiable changes to system parameters, that are well within measurement tolerance, we obtain excellent agreement between experiment and theory.

Given the excellent agreement between experiment and theory in the deflection–displacement results we can use the model to

**Table 2** Values of the initial distance of closest approach  $h_{init}$  in  $\mu\text{m}$  needed to fit the deflection–displacement data in Fig. 4

Scan rate/ $\mu\text{m s}^{-1}$	1	3	10	30
Drop S	1.96	1.86	1.86	1.85
Drop M	1.78	1.78	1.70	1.72
Drop L	1.90	1.85	1.85	1.90

infer information about the dynamics of drop behaviour during interaction that is otherwise not accessible by current experimental techniques. In Fig. 5, we show the time evolution of the drop shapes during interaction for size ratios of 3 (Drop S) and 20 (Drop L) at a scan rate of  $30 \mu\text{m s}^{-1}$ . When the interaction zone between the drops is large, the lower Laplace pressure of the larger drop allows it to deform more as it wraps itself around the smaller drop with an aqueous film of almost constant thickness separating the two drops (Fig. 6). For the small drop-size ratio (Drop S), shortly after the retraction commences the film develops a dimple so that the minimum of the film thickness is no longer at the axial centre  $r = 0$  but is located at the small barrier rim at  $r > 1 \mu\text{m}$  (see Fig. 7b). Note also that when the

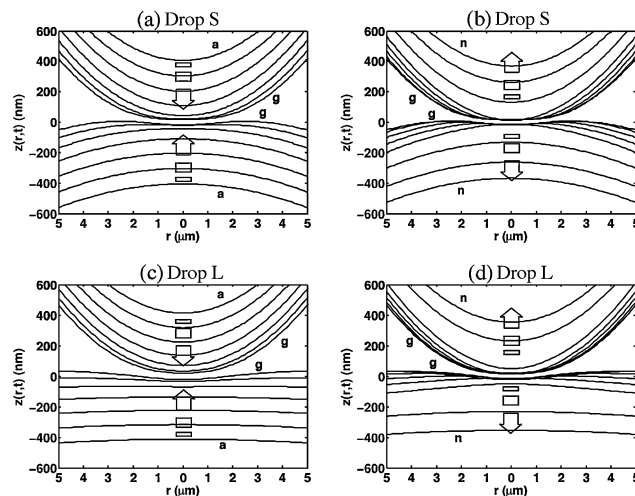


**Fig. 5** Variations of the profile  $z_c(r,t)$  for the drop on the cantilever (radius  $R_c = 25 \mu\text{m}$ ) and the profile  $z_s(r,t)$  for the drop on the substrate with radius  $R_{os} = 80 \mu\text{m}$  (Drop S) during (a) approach and (b) retract or with radius  $R_{os} = 513 \mu\text{m}$  (Drop L) during (c) approach and (d) retract. The drop-size ratios are approximately 3 and 20. The scan rate is  $30 \mu\text{m s}^{-1}$ . At each time step, the origin  $z = 0$  is taken to be at the mid-point between the two moving surfaces. The times for the profiles during approach are a–g: 0.034, 0.039, 0.045, 0.050, 0.056, 0.061, 0.067 s and during retraction are g–n: 0.067, 0.072, 0.078, 0.083, 0.089, 0.094, 0.100, 0.105 s.

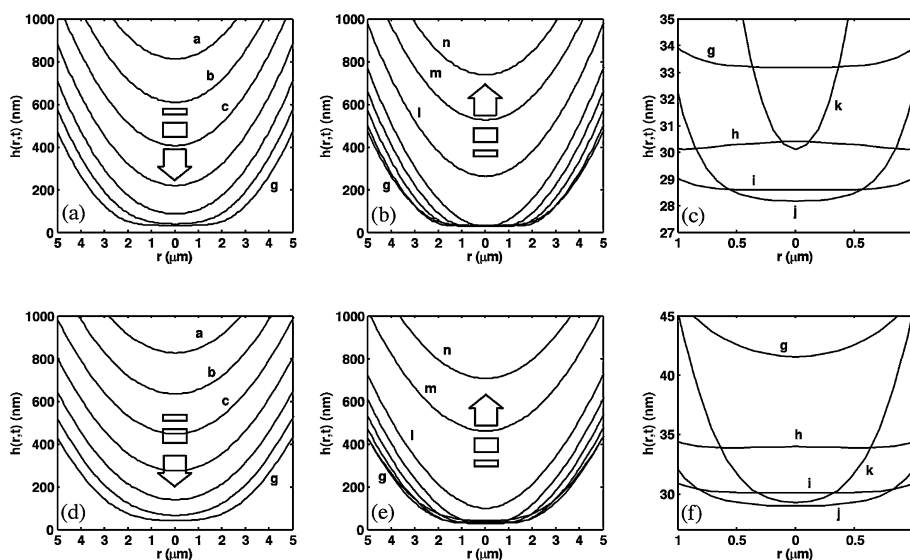


**Fig. 6** Variations of the aqueous film thickness  $h(r,t)$  for Drop S (top row) during approach (a) and retract (b) and (c) and Drop L (bottom row) during approach (d) and retract (e) and (f). The enlarged views in (c) and (f) show that the aqueous film becomes thinner immediately after the start of the retraction phase which starts at time (g) and reaches a minimum at time (j).

retraction commences at time (g), the dimple occurs at an intermediate time (h) and the film thickness first decreases until time (j) before it starts to increase as the drops eventually separate. This small dimpling event is qualitatively different from the familiar hydrodynamic dimpling that develops during film drainage when deformable surfaces are being pushed together—the present dimple develops after the drops have started to be pulled apart while the average film thickness is decreasing during the initial phase of the retraction process. An explanation of this process can be found by studying the pressure variation during this time.

In Fig. 7, we show variations of the hydrodynamic and disjoining pressure for Drop S with size ratio  $\approx 3$ . During the approach phase between times (f) and (g) (Fig. 7a), the intervening aqueous film with profile  $h(r,t)$  starts to flatten and drainage of this film slows down. This is reflected in the decrease in the magnitude of the hydrodynamic pressure  $p(r,t)$  between times (f) and (g). As the aqueous film flattens, the sum of the hydrodynamic and disjoining pressure,  $[p(r,t) + \Pi(h(r,t))]$  must, according to the Young–Laplace equation, eqn (4), balance the Laplace pressure of the drop  $\sim (2\sigma/R_0)$ . At the start of the retract phase, the hydrodynamic pressure decreases most rapidly near the edge of the flat film as seen in the change of  $p(r,t)$  between times (g) and (h) where both its magnitude and radial extent decrease. However, the aqueous film is still flat and so in order for  $[p(r,t) + \Pi(h(r,t))]$  to balance the Laplace pressure of the drop  $\sim (2\sigma/R_0)$ , this decrease in the hydrodynamic pressure  $p(r,t)$  must be balanced by a corresponding increase in the disjoining pressure  $\Pi(h)$  from time (g) to (h). Since  $\Pi(h)$ , which is due to electrical double layer repulsion, increases with decreasing  $h$ , an increase in  $\Pi(h)$  must be accompanied by a decrease in the film thickness  $h$ , and this results in the observed change in  $\Pi(h)$  between times (g) and (h). The dimple in the film thickness at time (h) is also reflected in a minimum in  $\Pi$  at  $r = 0$  with a corresponding local maximum in  $h(r,t)$ . The shoulder in the disjoining pressure  $\Pi$  near the edge of the flat film,  $r \approx 1\text{--}2 \mu\text{m}$ , arises

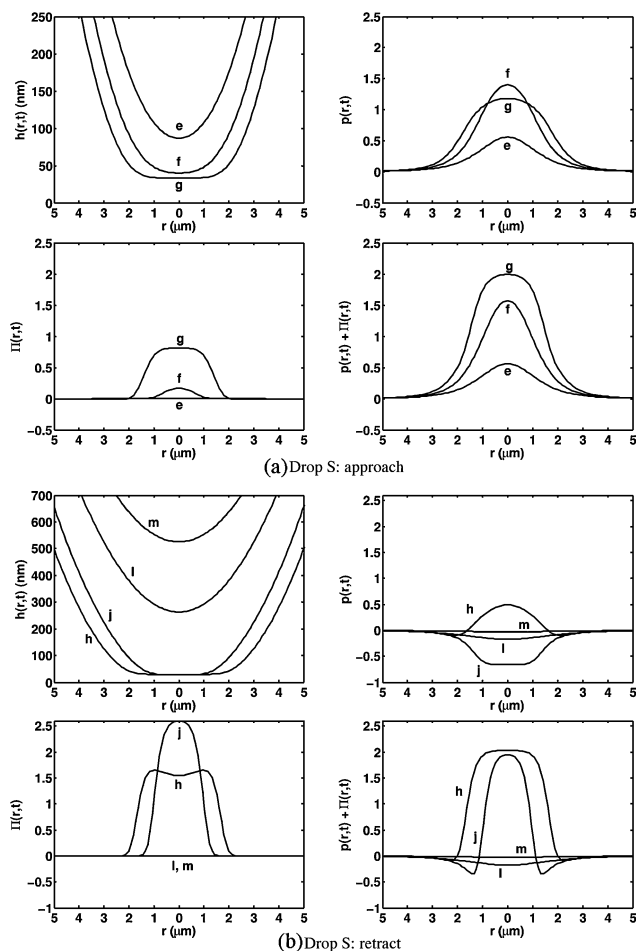


**Fig. 7** Variations of the aqueous film thickness  $h(r,t)$ , hydrodynamic pressure  $p(r,t)$  and disjoining pressure  $\Pi(r,t)$  and total dynamic disjoining pressure ( $p + \Pi$ ) during the (a) approach times a–g and (b) retract times h–l defined in Fig. 5. Both pressures are scaled by  $(\sigma/R_0)$ . The drop radius on the cantilever is  $R_{0c} = 25 \mu\text{m}$  and the drop on the substrate is Drop S:  $R_{0s} = 80 \mu\text{m}$ . The scan rate is  $30 \mu\text{m s}^{-1}$ .

because of the significant decreases in the magnitude and radial extent of the hydrodynamic pressure,  $p$ .

At its largest, the aqueous film between the drops has a uniform thickness of around 28 nm and a radial dimension of around 2  $\mu\text{m}$  or about 8% of the radius of the small drop on the cantilever. Thus the extent of the deformation during interaction remains small on the scale of the drop size.

Due to the combination of deformability, disjoining pressures and hydrodynamic interactions, the instantaneous local velocities of the surfaces of the interacting drops can take on different magnitudes and even signs compared to the velocity of the piezo drive. In Fig. 8a, the velocities of the two drops at  $r = 0$  and at  $r = r_{\text{max}}$  are shown as functions of time during an approach/retract cycle; and in Fig. 8b, the corresponding rate of change of the thickness of the aqueous film  $\partial h(r,t)/\partial t$  is shown. Velocities at other  $r$  positions are intermediate between these values. Up until  $t = 0.067$  s—times are labeled (a) to (g) for easy reference—we see that the surface velocity of the drop on the cantilever decreases in magnitude as hydrodynamic interactions begin to take effect. At the same time, the drop on the substrate also begins to retreat from the approaching drop on the cantilever, as indicated by its velocity becoming slightly negative. The film thickness is thinning during this time as  $\partial h(r,t)/\partial t$  is negative between times (a) to (g). The two surfaces attain the same velocity at  $r = 0$  after time (f). At time (g) the piezo drive

reverses direction. Between times (g) and (k), the surfaces at  $r = 0$  both move at the same velocity and the film thickness remains constant since  $\partial h(r,t)/\partial t$  is zero during this time interval. By comparing the velocities at  $r = 0$  and at  $r = r_{\text{max}}$  we see that only the apex of the drop on the substrate is in significant motion as its velocity at  $r = r_{\text{max}}$  remains small throughout. After time (k), the drop surfaces around  $r = 0$  start to separate. Note however that the magnitudes of both velocities attain a maximum as both drops exhibit a “velocity overshoot” after separation at time (l) before the velocity of the drop on the substrate returns to the scan rate and the drop on the cantilever returns to the quiescent state. This velocity overshoot phenomenon has been observed for interacting drops of similar size.<sup>22</sup>

In Fig. 9a we plot the interaction force  $F(t)$  as a function of the drop separation or aqueous film thickness  $h(0,t)$  at the axis of symmetry  $r = 0$ . The time points marked in Fig. 8 are indicated to facilitate comparison. This  $F(t)$  vs.  $h(0,t)$  graph should be viewed as a time sequence diagram from time (a) to time (n) rather than as a traditional force–separation curve. The reason is that this force is a non-conservative dynamic quantity which depends on separation and relative velocity. In the inset of Fig. 9a, the force is plotted as a function of the separation,  $Y$  between the base of the two interacting drops (see eqn (3) and Fig. 1) which removes the small effects in this case due to cantilever deflections. In Fig. 9b we show the variation of central

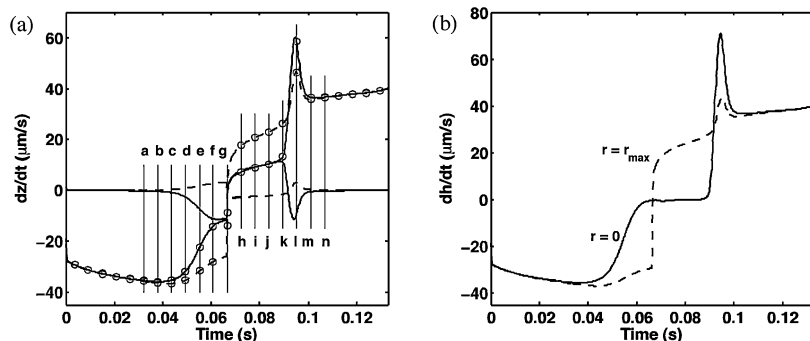


**Fig. 8** (a) Variations of the velocity  $\partial z_c(r,t)/\partial t$  of the surface of the drop on the cantilever at  $r = 0$  (full line with symbols), and at  $r = r_{\text{max}}$  (broken line with symbols) and of the velocity  $\partial z_s(r,t)/\partial t$  of the drop on the substrate at  $r = 0$  (full line), and at  $r = r_{\text{max}}$  (broken line). Velocities are designated as negative if motion is directed downwards towards the substrate in the AFM. (b) Variation of the film thinning rate  $\partial h(r,t)/\partial t$  with time at  $r = 0$  (full line) and at  $r = r_{\text{max}}$  (broken line). The radius of the drop on the substrate is Drop S:  $R_{\text{os}} = 80 \mu\text{m}$  and the scan rate is  $30 \mu\text{m s}^{-1}$ .

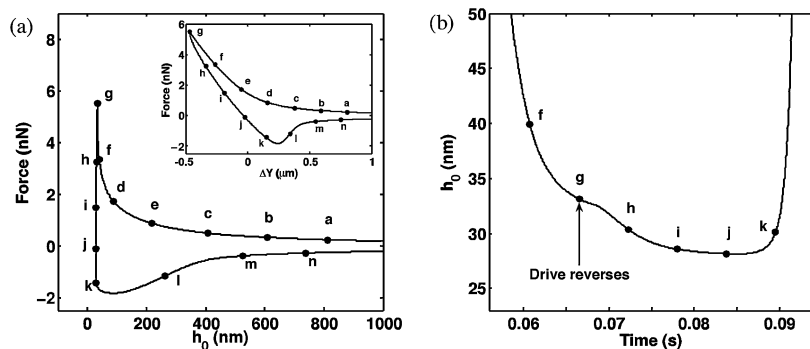


**Fig. 9** (a) The force  $F$  between two tetradecane drops as a function of the film thickness  $h_0 = h(0,t)$  at the axis of symmetry  $r = 0$ . Inset: the force plotted as a function of the separation  $\Delta Y$  between the base of the drops (see Fig. 1). (b) Variation of the film thickness  $h_0 = h(0,t)$  at the axis of symmetry  $r = 0$  as a function of time. The data are for Drop S ( $R_{\text{os}} = 80 \mu\text{m}$ ) on the substrate at a scan rate of  $30 \mu\text{m s}^{-1}$ .

thickness  $h(0,t)$  of the aqueous film with time. Here we observe the film thickness reaching its minimum value *after* the retract phase has started and the drops are being pulled apart as observed previously in Fig. 7 for hydrodynamic and disjoining pressure. The implication of this is that if the disjoining pressure has an attractive region at small separations that is only sampled by the drop during the retract phase, a coalescence instability may be induced *after* the drops are pulled apart as might happen in the case of drops subjected to an externally imposed hydrodynamic flow field.<sup>35</sup>

## 5. Discussion

The dynamic force between two oil drops of different size ratios between 3 and 20 has been studied by the AFM for scan rates up to  $30 \mu\text{m s}^{-1}$ . An accurate quantitative account of the observed hysteretic behaviour of the measured forces can be obtained from a model that includes the effects of colloidal forces, hydrodynamic interactions and droplet deformations. This model, based on continuum mechanics, provided additional quantitative information about the deformation dynamics of the thin aqueous film formed between the drops during interaction. By considering cantilever deflection *vs.* displacement data in comparing experiment and theory it was possible to deduce the drop-loaded spring constant of the cantilever without a separate calibration step. Due to the repulsive disjoining pressure that arises from electric double layer interactions between adsorbed surfactants at the oil/water interface, an aqueous film of thickness  $h_{\text{eq}} \approx 28 \text{ nm}$  separates the droplet interfaces as the larger drop with a lower Laplace pressure wraps about the smaller drop. This value of  $h_{\text{eq}}$  is determined by the film thickness when the disjoining pressure is equal to the Laplace pressure of the drops:  $\Pi(h_{\text{eq}}) = 2\sigma/R_0$ .

Detailed analysis of interfacial deformations revealed the development of a dimpling phenomenon in the aqueous film profile during the initial part of the retraction phase. This dimple arises from the combined effects of the rapid decrease in hydrodynamic pressure during the initial part of the retraction phase when the film remains relatively flat and the monotonic nature of the variation of the disjoining pressure with film thickness due to repulsive electrical double layer interactions.

Analysis of the aqueous film dynamics also shows that as the retract phase commences, the aqueous film thickness will initially decrease before it increases as the drops finally separate. This initial thinning can provide a destabilising mechanism for the initiation of droplet coalescence.

## Acknowledgements

This work has been supported in part by the Particulate Fluids Processing Centre, a Special Research Centre of the Australian Research Council. R. M. is supported by a University of Melbourne International Research Scholarship. D. C. is supported by a Visiting Professorship at the National University of Singapore and an adjunct appointment at the Institute of High Performance Computing, Singapore.

## References

- 1 W. A. Ducker, T. J. Senden and R. M. Pashley, *Nature*, 1991, **353**, 239–241.
- 2 W. A. Ducker, T. J. Senden and R. M. Pashley, *Langmuir*, 1992, **8**, 1831–1836.
- 3 P. M. Claesson, T. Ederth, V. Bergeron and M. W. Rutland, *Adv. Colloid Interface Sci.*, 1996, **67**, 119–184.
- 4 V. S. J. Craig, *Colloids Surf., A*, 1997, **129**(130), 75–94.
- 5 P. G. Hartley, *Colloid–Polym. Interact.*, 1999, 253–286.
- 6 W. A. Ducker, Z. Xu and J. N. Israelachvili, *Langmuir*, 1994, **10**, 3279–3289.
- 7 H.-J. Butt, *J. Colloid Interface Sci.*, 1994, **166**, 109–117.
- 8 P. Mulvaney, J. M. Perera, S. Biggs, F. Grieser and G. W. Stevens, *J. Colloid Interface Sci.*, 1996, **183**, 614–616.
- 9 P. G. Hartley, F. Grieser, P. Mulvaney and G. W. Stevens, *Langmuir*, 1999, **15**, 7282–7289.
- 10 S. A. Nespolo, D. Y. C. Chan, F. Grieser, P. G. Hartley and G. W. Stevens, *Langmuir*, 2003, **19**, 2124–2133.
- 11 R. R. Dagastine, D. C. Prieve and L. R. White, *J. Colloid Interface Sci.*, 2004, **269**, 84–96.
- 12 D. E. Aston and J. C. Berg, *J. Colloid Interface Sci.*, 2001, **235**, 162–169.
- 13 R. R. Dagastine, T. T. Chau, D. Y. C. Chan, G. W. Stevens and F. Grieser, *Faraday Discuss.*, 2005, **129**, 111–124.
- 14 L. Y. Clasohm, I. U. Vakarelski, R. R. Dagastine, D. Y. C. Chan, G. W. Stevens and F. Grieser, *Langmuir*, 2007, **23**, 9335–9340.
- 15 G. Gillies, C. A. Prestidge and P. Attard, *Langmuir*, 2002, **18**, 1674–1679.
- 16 B. A. Snyder, D. E. Aston and J. C. Berg, *Langmuir*, 1997, **13**, 590–593.
- 17 R. R. Dagastine, T. T. Chau, D. Y. C. Chan, G. W. Stevens and F. Grieser, World Congress of Chemical Engineering, 7th, Glasgow, United Kingdom, July 10–14, 2005, Institute of Chemical Engineers, Rugby, UK, 2005, pp. 86500/86501–86500/86509.
- 18 D. E. Aston and J. C. Berg, *Ind. Eng. Chem. Res.*, 2002, **41**, 389–396.
- 19 G. B. Webber, R. Manica, S. A. Edwards, S. L. Carnie, G. W. Stevens, F. Grieser, R. R. Dagastine and D. Y. C. Chan, *J. Phys. Chem. C*, 2007, **112**, 567–574.
- 20 R. R. Dagastine, R. Manica, S. L. Carnie, D. Y. C. Chan, G. W. Stevens and F. Grieser, *Science*, 2006, **313**, 210–213.
- 21 R. R. Dagastine, G. W. Stevens, D. Y. C. Chan and F. Grieser, *J. Colloid Interface Sci.*, 2004, **273**, 339–342.
- 22 S. L. Carnie, D. Y. C. Chan, C. Lewis, R. Manica and R. R. Dagastine, *Langmuir*, 2005, **21**, 2912–2922.
- 23 S. L. Carnie, D. Y. C. Chan and R. Manica, *ANZIAM J.*, 2005, **46**(E), C808–C819.
- 24 I. U. Vakarelski, S. A. Edwards, R. R. Dagastine, D. Y. C. Chan, G. W. Stevens and F. Grieser, *Rev. Sci. Instrum.*, 2007, **78**, 116102/116101–116102/116103.
- 25 J. L. Hutter and J. Bechhoefer, *Rev. Sci. Instrum.*, 1993, **64**, 1868–1873.
- 26 J. F. Wall, F. Grieser and H. F. Zukoski, *J. Chem. Soc., Faraday Trans.*, 1997, **93**, 4017–4020.
- 27 D. Y. C. Chan, R. R. Dagastine and L. R. White, *J. Colloid Interface Sci.*, 2001, **236**, 141–154.
- 28 R. Manica, J. N. Connor, R. R. Dagastine, S. L. Carnie, R. G. Horn and D. Y. C. Chan, *Phys. Fluids*, 2007, **20**, 032101.
- 29 J. C. Baygents and D. A. Saville, *J. Chem. Soc., Faraday Trans.*, 1991, **87**, 1883–1898.
- 30 E. Klaseboer, J. P. Chevaillier, C. Gourdon and O. Masbernat, *J. Colloid Interface Sci.*, 2000, **229**, 274–285.
- 31 S. A. Nespolo, M. A. Bevan, D. Y. C. Chan, F. Grieser and G. W. Stevens, *Langmuir*, 2001, **17**, 7210–7218.
- 32 S. G. Yiantsios and R. H. Davis, *J. Fluid Mech.*, 1990, **217**, 547–573.
- 33 D. C. Bardos, *Surf. Sci.*, 2002, **517**, 157–176.
- 34 R. R. Dagastine and L. R. White, *J. Colloid Interface Sci.*, 2002, **247**, 310–320.
- 35 S. Guido and M. Simeone, *J. Fluid Mech.*, 1998, **357**, 1–20.